Medicine in Novel Technology and Devices 4 (2019) 100027

Contents lists available at ScienceDirect

Medicine in Novel Technology and Devices

journal homepage: www.journals.elsevier.com/medicine-in-novel-technology-and-devices/

Research Paper

A pilot study of aortic hemodynamics before and after thoracic endovascular repair with a double-branched endograft

Yu Zhu [a], Wenbo Zhan [a], Mohamad Hamady [b], Xiao Yun Xu [a,*]

[a] Department of Chemical Engineering, Imperial College London, UK
[b] Department of Interventional Radiology, St Mary's Hospital, Imperial College Healthcare NHS Trust, London, UK

ARTICLE INFO

Keywords:
Thoracic endovascular aortic repair (TEVAR)
Aortic arch
Branched endograft
Blood flow
Computational fluid dynamics

ABSTRACT

Branched endografts have been developed to treat complex pathology in the aortic arch and ascending aorta. This study aims to evaluate the haemodynamic performance of a double-branched thoracic endograft by detailed comparison of flow patterns and wall shear stress in the aorta and supra-aortic branches before and after stent-graft implantation. Pre- and post-intervention CT images were acquired from two patients who underwent thoracic endovascular aortic repair (TEVAR) with a double-branched endograft for thoracic aortic aneurysms. These images were used to reconstruct patient-specific models, which were analysed using computational fluid dynamics employing physiologically realistic boundary conditions. Our results showed that there was sufficient blood perfusion through the arch branches. The presence of inner tunnels caused flow derangement and asymmetric wall shear stress in the ascending aorta, where shear range index was up to 6 times higher than in the pre-intervention model. Wall shear stress in the aortic arch increased considerably after intervention as a result of accelerated flow. The maximum flow-induced displacement forces on the branched endografts were around 22 N for both patients, which was below the threshold for device migration. Results from this pilot study demonstrated that aortic flow patterns were significantly altered by the branched endograft which caused increased spatial variation of wall shear stress in the ascending aorta and the arch. Although no obvious adverse hemodynamic features were found immediately after intervention for the cases we analysed, follow-up studies will be needed to assess durability of the device.

1. Introduction

Thoracic endovascular aortic repair (TEVAR) has been developed over 2 decades and has become one of the most popular choices for treating descending thoracic aortic diseases. In recent years, its application has been extended more proximally in the aorta, if there is a suitable landing zone, to treat pathology in the aortic arch and ascending aorta. However, traditional stent-grafts are too stiff to conform to the inner curvature of the aortic arch, which may result in a wedge-shaped gap between the aortic wall and the under surface of the graft, known as bird-beak configuration [1]. To overcome this challenge, branched endografts have been developed, including single-branched and multi-branched endografts. One such example is the Relay thoracic stent-graft system developed by Bolton Medical (Sunrise, FL, US), which was designed to conform into the tight aortic curvature in order to avoid the bird-beak configuration [2].

It is well recognised that blood flow in aortic aneurysms is highly disturbed, with the presence of flow recirculation and strong vortices [3,4]. Insertion of a branched stent-graft may further increase the complexity of the flow [5]. In order to provide a non-invasive evaluation of aortic flow patterns, computational fluid dynamics (CFD) has been employed for its ability to offer comprehensive insights into spatial-temporal variations of the flow [6]. When applied to patient-specific aorta geometry reconstructed from medical images together with physiological boundary conditions, CFD allows quantitative assessment of cardiovascular flow with good accuracy [7–9].

Computational studies have been conducted on blood flow in the human aortic arch, where geometrical complexities such as tortuosity, non-planarity and the presence of supra-aortic branches are included to understand their effects on blood flow [10,11]. CFD simulations have also been performed to investigate the role of blood flow patterns and hemodynamic parameters in pathological changes of the aorta [12–14]. In addition, fluid-structure interaction (FSI) simulations have been performed on the aortic arch with and without an aneurysm [15–17]. Most

* Corresponding author. Department of Chemical Engineering Imperial College London London, SW7 2AZ, UK.
E-mail address: yun.xu@imperial.ac.uk (X.Y. Xu).

https://doi.org/10.1016/j.mednotd.2020.100027
Received 25 October 2019; Received in revised form 5 December 2019; Accepted 26 December 2019

recently, Miyazaki et al. [18] applied different turbulence models to evaluate the effect of turbulence on blood flow in the aortic arch by comparing 4D flow magnetic resonance imaging (MRI) measurements with CFD simulation results. While most of previous computational studies focused on flow in normal and diseased aortic arch, only a few considered the influence of endografts [1,19–22]. Nardi et al. [19], among others, compared the hemodynamic performance of different endovascular procedures for the treatment of aortic arch aneurysm using idealised geometric models. Van Bogerijen et al. [1] employed patient-specific models to examine the effect of TEVAR with a focus on the bird-beak configuration. Patient-specific analysis of flow in double-branched aortic arch endograft has not been reported in the literature.

Detailed knowledge of the hemodynamic performance of double-branched thoracic endografts is important for assessing the risk of post-intervention complications and long-term durability of the device. The most common and potentially life-threatening post-TEVAR complications include endoleaks, distal migration of the device, and thrombus formation within the stent-graft. Among all types of endoleaks, type I endoleaks occur more frequently in TEVAR, resulting from poor sealing between the device and the aortic wall [23]. Distal migration of the device can also result in type I endoleak, thereby increasing the risk of aneurysm rupture. Thrombus formation within the stent-graft can reduce or even block blood perfusion to the supra aortic branches, which may lead to ischaemia. All these complications are associated with abnormal flow behaviour and flow induced forces. For example, high values of shear stress may cause platelet activation, whereas low wall shear stress and long residence time can promote platelet adhesion and thrombus formation [24,25]. Large displacement forces acting on the stent-graft are the main cause for device migration [26]. However, these flow-related parameters could not be measured directly in vivo. Through this pilot study we aim to provide the first detailed evaluation of the hemodynamic performance of double-branched thoracic endografts by means of patient-specific CFD analysis. Pre- and post-intervention geometries were reconstructed from the CT images acquired before and after the TEVAR procedure. These were then coupled with physiologically realistic boundary conditions. Hemodynamic performance was evaluated in terms of flow pattern, wall shear stress (WSS) related indices and displacement forces (DF). By comparing pre- and post-intervention flow distributions, it would be possible to assess the level of blood perfusion through the arch branches. Quantitative analysis of WSS-related indices would help predict the likelihood of thrombus formation within the endograft, whilst quantification of DF experienced by the endograft would allow us to evaluate the risk of device migration.

2. Methods

2.1. Branched stent-graft and CT scan

The studied branched device (Bolton Medical, Sunrise, FL, US) comprises a main covered stent-graft to take the pressure off the vessel wall of the aortic arch and two attached tunnels to channel the blood directly into the innominate artery (IA) and left common carotid artery (LCCA). Patient 1 was treated with an endograft with 2 inner branches of equal diameters (15 mm) while the inner branch to the LCCA of patient 2 had a smaller diameter (9 mm) compared to the IA (17 mm). For both patients, the left subclavian artery (LSCA) was covered at the root, and a separate bypass procedure was performed to supply blood to the LSCA from the LCCA. CT images for both patients were acquired (1.25 mm slice thickness and 0.675 mm/pixel in-plane resolution) with a Discovery CT750 HD scanner (GE Healthcare, Chicago, IL, US), at voltages of 100 KV and 120 KV, for the pre- and post-intervention scans, respectively. Formal ethical approval was not required for this limited retrospective and anonymised study.

2.2. Model geometry

The multislice transverse images were processed using image analysis software MIMICS 20.0 (Materialise, Leuven, Belgium), with luminal surface being segmented based on the local signal intensity. The segmented 2D masks were then smoothed by the Discrete Gaussian filter based on a linear smoothing enhancement algorithm. 3D reconstruction was performed through surface rendering, which involved delineating lumen contours for each slice in the transverse plane and generating a 3D surface by superimposing and lofting these contours in the coronal plane. Finally, a cubic spline algorithm was applied for 3D smoothing. The representative CT images and reconstructed luminal surfaces of the pre- and post-intervention models are presented in Fig. 1. In the reconstructed models, the presence of stent wires was ignored and the inner surface of the stent-graft was assumed to be smooth. Blooming artefacts due to the presence of thin stent wires were not a major concern here as the stent mesh was not very dense and the lumen diameter is fairly large.

The 3D geometries were then imported into ANSYS ICEM CFD (ANSYS, Canonsburg, PA, US) to generate computational mesh, which consisted of tetrahedral elements in the core region and locally refined hexahedral elements in the sheared boundary layer for accurate prediction of hemodynamic wall parameters. The viscous sub-layer (approximately 1 mm thick) was divided into a minimum of 10 prismatic elements to ensure that the dimensionless height of the near wall elements, $y+$, was less than 1. Mesh sensitivity tests were carried out, starting with a mesh containing approximately 1 million elements. The final adopted meshes consisted of around 3 and 8.5 million elements for the pre- and post-intervention aortas, respectively. Results were considered to be grid independent when differences in velocity and WSS were less than 2% between the adopted mesh and a finer mesh. A fixed timestep of 0.001s was chosen based on a similar sensitivity test on timestep size.

2.3. Flow model

The conservation of mass and momentum equations for an incompressible, Newtonian fluid were used to describe the pulsatile blood flow. In addition, the hybrid k-ε/k-ω correlation-based shear stress transport transitional model (SST-Tran) was applied to capture transitional/turbulent flow characteristics [27]. Blood was assumed to have a constant density of 1060 kg/m^3 and dynamic viscosity of 4 mPa s.

2.4. Boundary conditions

Physiological boundary conditions were employed in order to produce clinically relevant results. Since patient-specific flow information was not available, velocity waveform acquired from a patient with thoracic aortic aneurysm was adopted [16] and scaled according to the inlet area of each patient, yielding a cycle-averaged inlet velocity of 0.1 m/s for both patients. This corresponds to a cardiac output of 5 L/min for patient 1 and 3.4 L/min for patient 2, both are within the physiological range [28]. A schematic of the computational model and the applied inflow waveform can be found in Fig. 2.

At each model outlet, a 3-element Windkessel model (3-EWM) was applied in order to provide physiological outflow boundary conditions. The 3-EWM describes an arterial system by using arterial compliance (C), proximal impedance of the aorta (R1) and peripheral resistance (R2). It is capable of capturing the main characteristics of arterial blood pressure waveform [29]. The assumption of rigid stent-graft walls was made where no-slip boundary conditions were imposed. To calculate the 3-EWM parameters, pressure waveforms at each outlet were adopted from the literature [30] and the corresponding cycle-averaged pressures were evaluated as: 105 mmHg, 104 mmHg, 103 mmHg, and 103 mmHg, for the IA, LCCA, LSCA and descending aorta (DA), respectively. For the post-intervention model, the outlet boundary conditions were modified to account for the fact that the LSCA was covered at the root and its blood

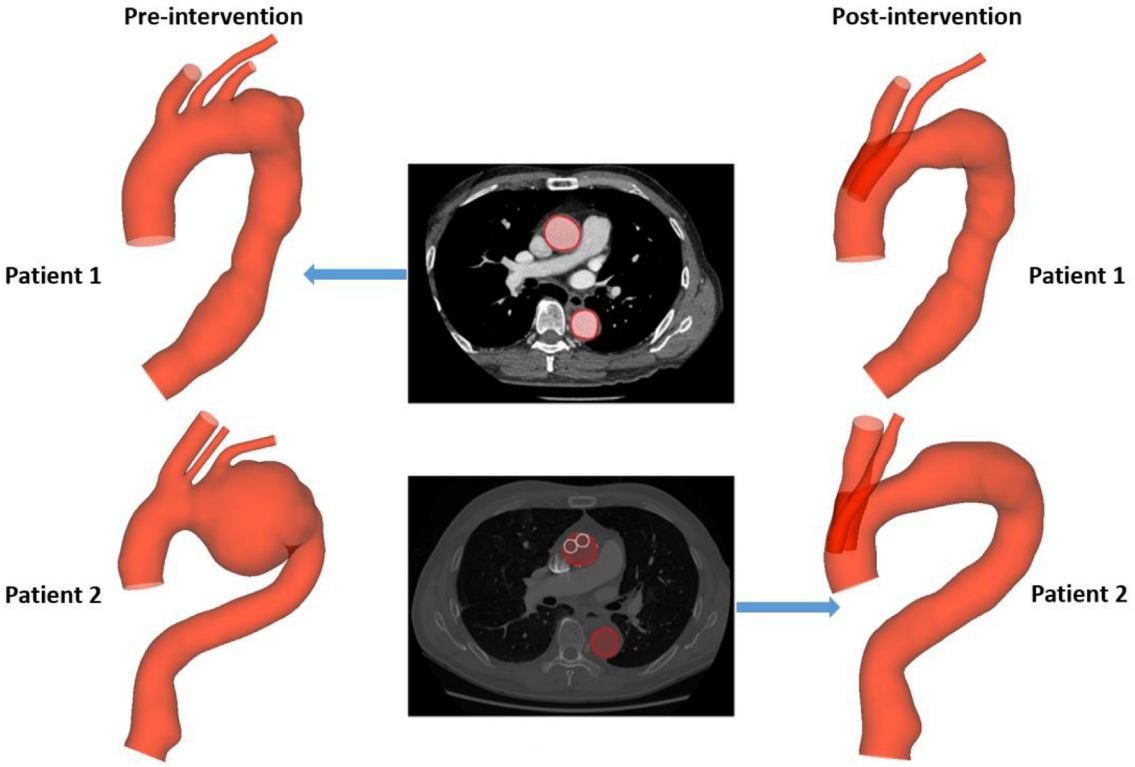

Fig. 1. Two patient-specific models reconstructed from pre- and post-intervention CT images.

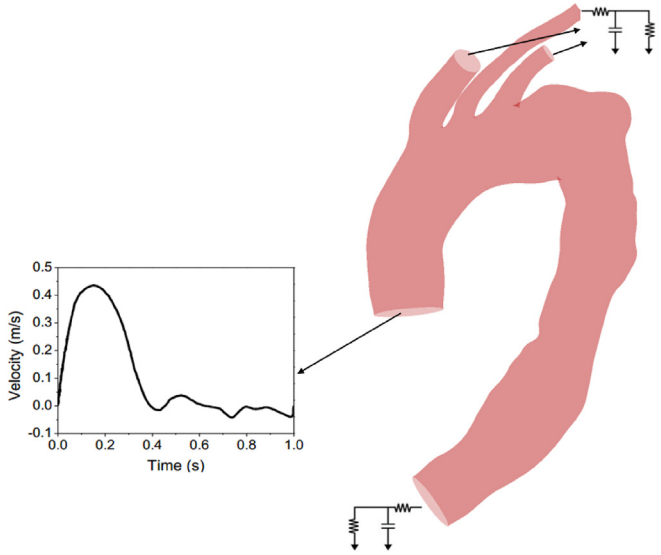

Fig. 2. Schematic of the computational model employed in this study. Velocity waveform was prescribed at the inlet, while a 3-element Windkessel model was applied at all outlets.

supply was rerouted from the LCCA via a separate bypass procedure. As shown in Fig. 3, the total downstream resistance at the LCCA outlet was calculated by combining the pre-intervention resistance for the LCCA ($R_{Pre\text{-}LCCA}$) and LSCA ($R_{Pre\text{-}LSCA}$) [31]:

$$1/R_{Post-LCCA} = 1/R_{Pre-LCCA} + 1/R_{Pre-LSCA}$$

The obtained resistance and compliance values are summarised in Table 1.

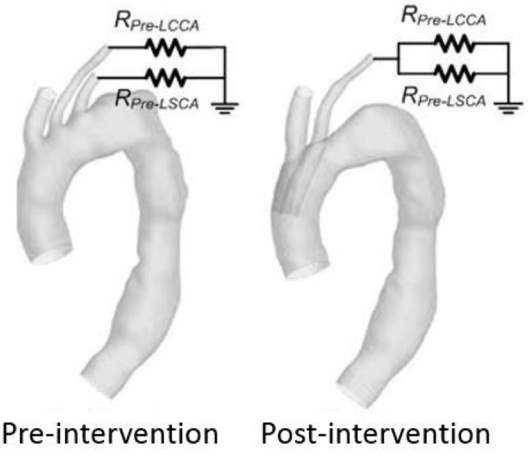

Fig. 3. Schematic diagram showing resistance at LCCA and LSCA in the pre- and post-intervention models.

2.5. Computational details

The governing equations were solved by means of ANSYS CFX 15 (ANSYS, Canonsburg, PA, US), which is a finite volume based CFD code. Spatial and temporal discretisations were performed by adopting the second order accurate advection scheme and the second order implicit backward Euler scheme, respectively. Convergence of simulations was controlled by setting the residual tolerance as 1×10^{-5}. Each simulation was performed for three cardiac cycles when solutions for both velocity and pressure became periodic, and the differences in systolic pressure between the second and third cardiac cycle were less than 2% at every outlet. Three cardiac cycles are usually considered sufficient to achieve a periodic solution as demonstrated in similar studies [5,8,26,32]. Numerical results of the last cycle were analysed using ANSYS CFD-Post 15

Table 1
Windkessel parameters for all model outlets.

		Patient 1			Patient 2		
		R1 [10^8 Pa s m^{-3}]	R2 [10^8 Pa s m^{-3}]	C [10^{-9} m^3 Pa^{-1}]	R1 [10^8 Pa s m^{-3}]	R2 [10^8 Pa s m^{-3}]	C [10^{-9} m^3 Pa^{-1}]
Pre-intervention	IA	0.40	8.94	1.92	0.39	10.86	1.59
	LCCA	1.86	31.51	0.54	3.92	79.01	0.22
	LSCA	1.23	22.32	0.76	2.30	50.00	0.34
	DA	0.08	2.27	7.62	0.07	3.43	5.11
Post-intervention	IA	0.49	8.86	1.92	0.26	10.99	1.59
	LCCA	2.21	11.60	1.30	2.73	29.34	0.56
	DA	0.08	2.27	7.62	0.07	3.43	5.11

(ANSYS, Canonsburg, PA, US) and CEI Ensight 10 (CEI Inc, Apex, NC, US).

2.6. Hemodynamic indices

Wall shear stress (WSS) refers to the tangential force generated by blood flow on the endothelial luminal surface. Owing to its strong associations with thrombus formation and aneurysm growth and the fact that these processes are much slower compared to the pulsatile cycle period, WSS is usually evaluated in terms of time-averaged wall shear stress (TAWSS), defined as

$$TAWSS = \frac{1}{T}\int_0^T WSS \cdot dt \tag{1}$$

where T is the duration of a cardiac cycle, and t is time. In addition, circumferential wall shear stress (CWSS) and shear range index (SRI) were evaluated to quantify the extent of local derangement at the vessel wall [33].

$$SRI = \frac{\max[CWSS_{max}(\theta,t) - CWSS_{min}(\theta,t)}{TACWSS} \tag{2}$$

where $CWSS_{max}$ (θ,t) and $CWSS_{min}(\theta,t)$ represent the maximum and minimum WSS along the circumference of a cross-section, respectively. TACWSS is the temporal and circumferential averaged WSS at a given cross-section.

The displacement force was calculated by integrating pressure and WSS over the entire surface of the endograft. It is defined as [26]:

$$F_{d,i} = \int_{A,i}^{1} p \; dA + \int_{A,i}^{1}\left(-\mu\frac{\partial\vec{v_t}}{\partial\hat{n}}\right) dA \tag{3}$$

where the first term represents the pressure force and the second term represents the WSS force. A is the area of the endograft wall, and i refers to x, y and z in Cartesian coordinates. $\vec{v_t}$ is the tangential velocity with respect to the unit normal $\hat{n}$ for each wall element and μ is the blood viscosity. The magnitude of displacement force F_d is given by:

$$|F_d| = \sqrt{(F_{d,x})^2 + (F_{d,y})^2 + (F_{d,z})^2} \tag{4}$$

3. Results

3.1. Anatomical features

As shown in Fig. 1, the pre- and post-intervention geometries differed mainly in the arch for both patients. In the post-intervention model, two built-in tunnels were attached to the main graft body, through which separate stents were retrogradely inserted into the IA and LCCA, with entry to the LSCA being blocked from its origin. Lumen diameters were measured at eight selected locations to evaluate changes in aorta morphology after the intervention, and the results are summarised in Table 2. All locations were matched between the pre- and post-intervention geometries by measuring the distance along the respective centreline, which could be achieved in Mimics.

Comparisons showed that, apart from the obvious reduction in diameters in the regions where the aneurysms were located, there was no change in the ascending and descending aortas for both patients. Diameters of the IA and LCCA root were larger after intervention, with patient 2 showing a more pronounced increase in LCCA diameter.

3.1.1. Flow patterns

Instantaneous velocity streamlines in the pre- and post-intervention models were compared at three characteristic time points, namely, peak systole (0.15 s), mid-systolic deceleration (0.29 s) and diastole (0.74 s). As shown in Fig. 4a&b, aortic flow patterns for both patients altered significantly after intervention in response to changes in lumen morphology. Blood flow was more organised post-intervention as the

Table 2
Comparison of lumen diameters (mm) between the pre- and post-intervention models.

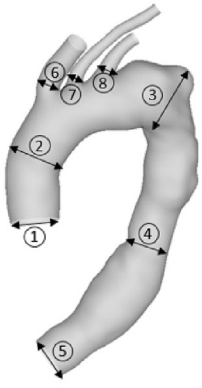

	Patient 1			Patient 2	
	Pre-intervention (mm)	Post-intervention (mm)		Pre-intervention (mm)	Post-intervention (mm)
①	32	32	①	27	27
②	35	35	②	28	28
③	47	37	③	69	33
④	30	30	④	23	23
⑤	29	29	⑤	31	31
⑥	14	15	⑥	14.6	15.7
⑦	7.5	8.5	⑦	5.3	8.5
⑧	9.5	-	⑧	6.7	-

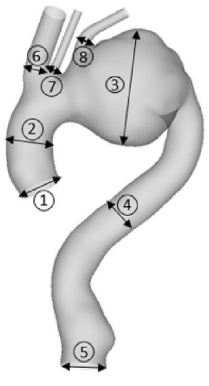

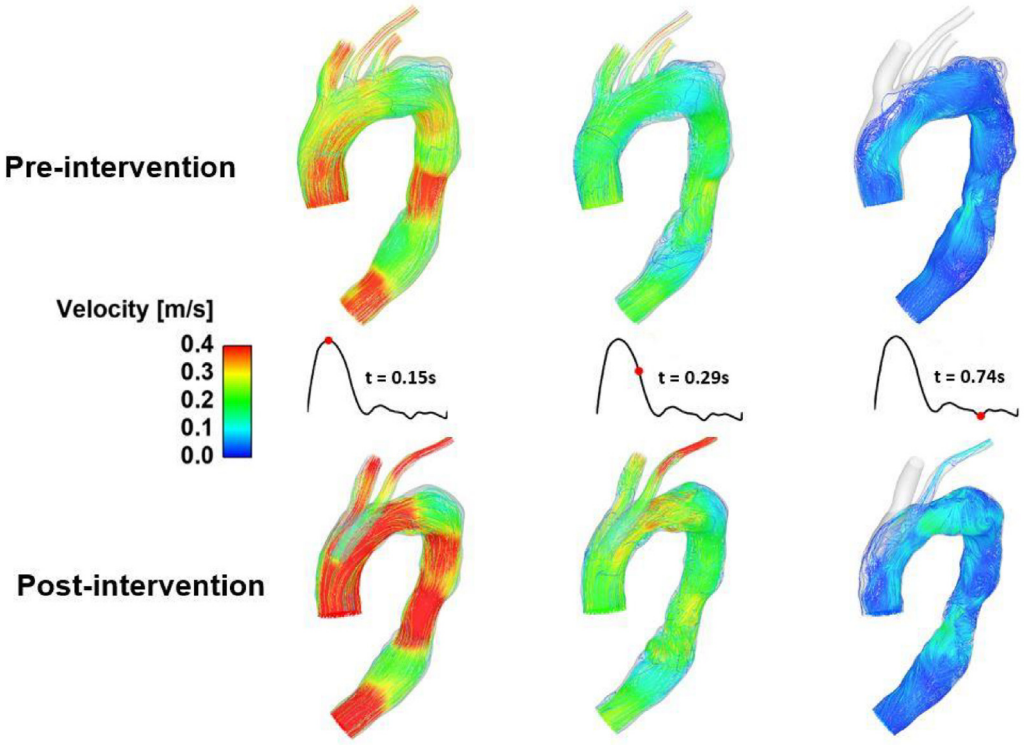

(a) Patient 1

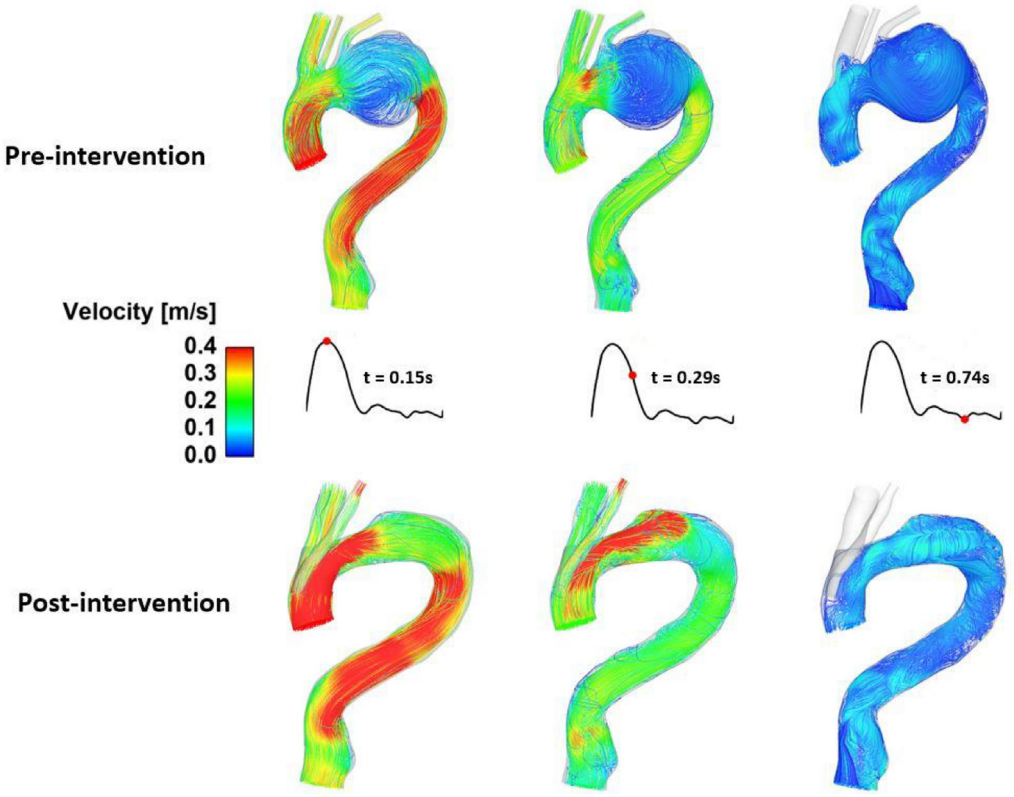

(b) Patient 2

Fig. 4. Comparisons of instantaneous velocity streamline in pre- and post-intervention models of (a) patient 1 and (b) patient 2.

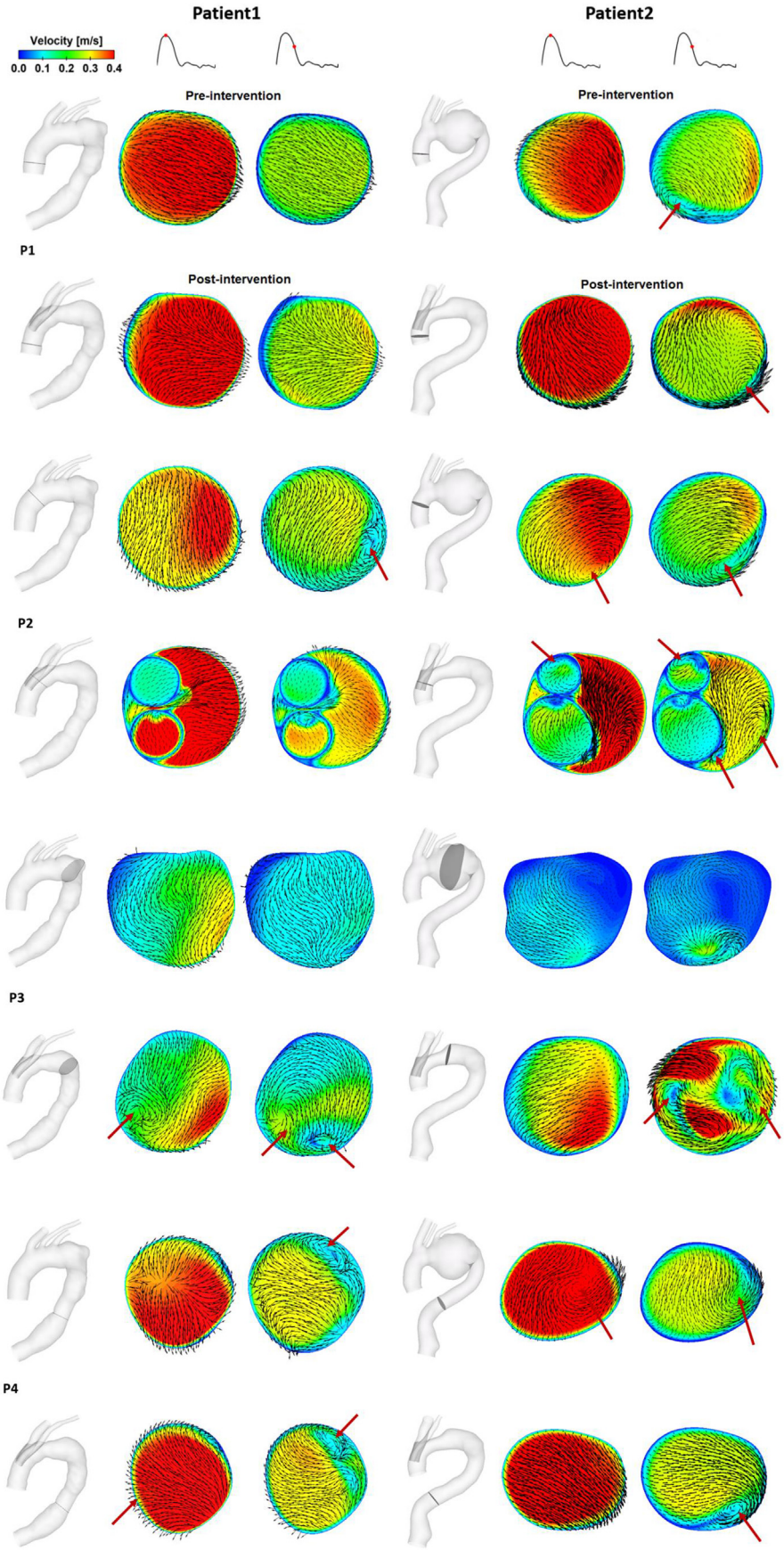

Fig. 5. a. Comparison of axial velocity contours along with in-plane velocity vectors before and after intervention in the main aortas of patient 1 (left) and patient 2 (right). b. Comparison of axial velocity contours along with in-plane velocity vectors before and after intervention in the IA of patient 1 (left) and patient 2 (right). c. Comparison of axial velocity contours along with in-plane velocity vectors before and after intervention in the LCCA of patient 1 (left) and patient 2 (right).

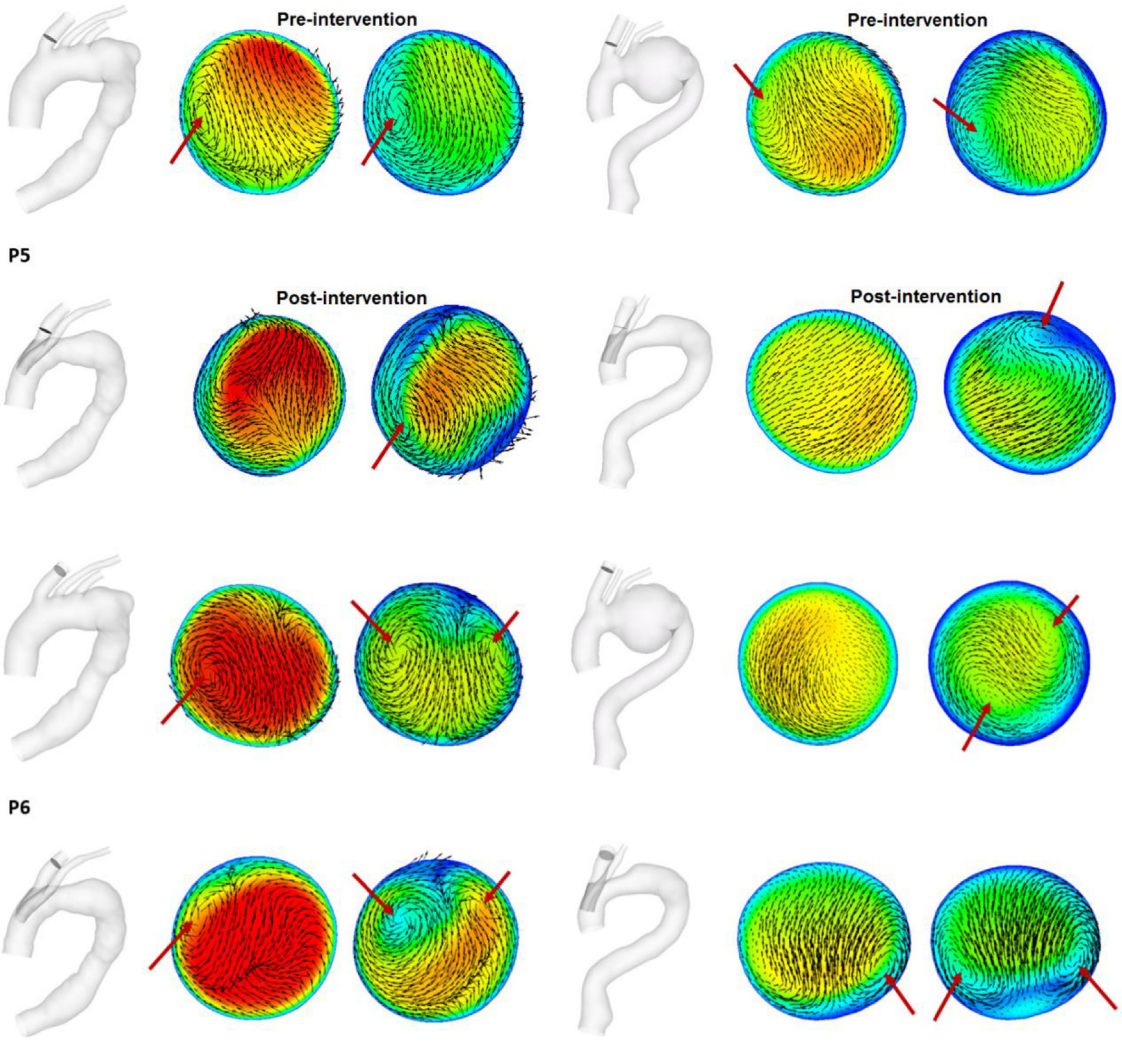

Fig. 5. (*continued*).

aneurysm was repaired. Blood velocities increased in the ascending aorta and the arch due to the presence of the inner tunnels. Flow in the LCCA increased in order to meet the demand of both LCCA and LSCA. As expected, the diastolic phase was dominated by slow and recirculating flow in both pre- and post-intervention aortas.

Eight cross-sectional planes were selected along the centreline of each aorta (P1–P4), the IA (P5 & P6) and the LCCA (P7 & P8) for detailed comparisons of flow and WSS. Through-plane velocity contours along with in-plane velocity vectors at these planes were compared before and after intervention, as illustrated in Fig. 5a–c, where the right hand side of each cross-sectional image corresponds to the inner curvature of the aorta and vortical flow structures are indicated by red arrows. For both patients, flow in the proximal ascending aorta (P1) hardly changed after the intervention, but this was completely different at P2 where the presence of the inner tunnels caused part of the aortic flow to be channelled into the IA and LCCA after intervention, while entry to the LSCA was blocked. Insertion of the stent-graft reduced the lumen area and thus accelerated blood flow in the posterior region but blocked flow in the anterior part. This stagnant region is likely to be thrombosed over time which may further obstruct the lumen. It can be seen clearly at P2 that patient 1 had a device with equal diameter inner tunnels, while patient 2 had a smaller inner branch to the LCCA. Patient 1 had a much higher blood velocity in the inner IA channel than LCCA when compared to patient 2. Geometric variations in the aneurysm sac (P3) changed local flow patterns after intervention, where vortical flow could be seen in systole. Flow in the descending aorta (P4) was similar before and after intervention.

Flow patterns in the arch branches were compared at two locations: (1) proximal region of the IA (P5) and LCCA (P7); and (2) distal region of the IA (P6) and LCCA (P8). It can be seen that velocity was higher in the IA than LCCA in the pre-intervention models of both patients, but more obvious for patient 1. These were the same for the post–intervention models, but only in the proximal regions (P5, P7). For both patients, blood flow in the LCCA (P7, P8) accelerated distally due to vessel tapering. The effect of tapering was more obvious in the LCCA than in IA.

3.2. *Wall shear stress*

Fig. 6 shows the predicted TAWSS contours, and it is clear that after intervention the magnitude of TAWSS increased throughout the aorta for both patients, as a result of accelerated flow in the arch and the distal LCCA. More detailed comparisons are shown in Fig. 7, where the mean circumferential WSS was plotted as a function of time at the pre-defined locations (P1–P8). For both patients, although temporal variations of circumferential WSS exhibited similar shapes before and after intervention, implantation of the branched stent-graft increased the magnitude of WSS in the systolic phase except for the proximal LCCA (P7) of patient 2, where higher WSS was found in the pre-intervention model. In diastole, however, the results were comparable except for P3 of both patients, where the post-intervention WSS was higher throughout the cardiac

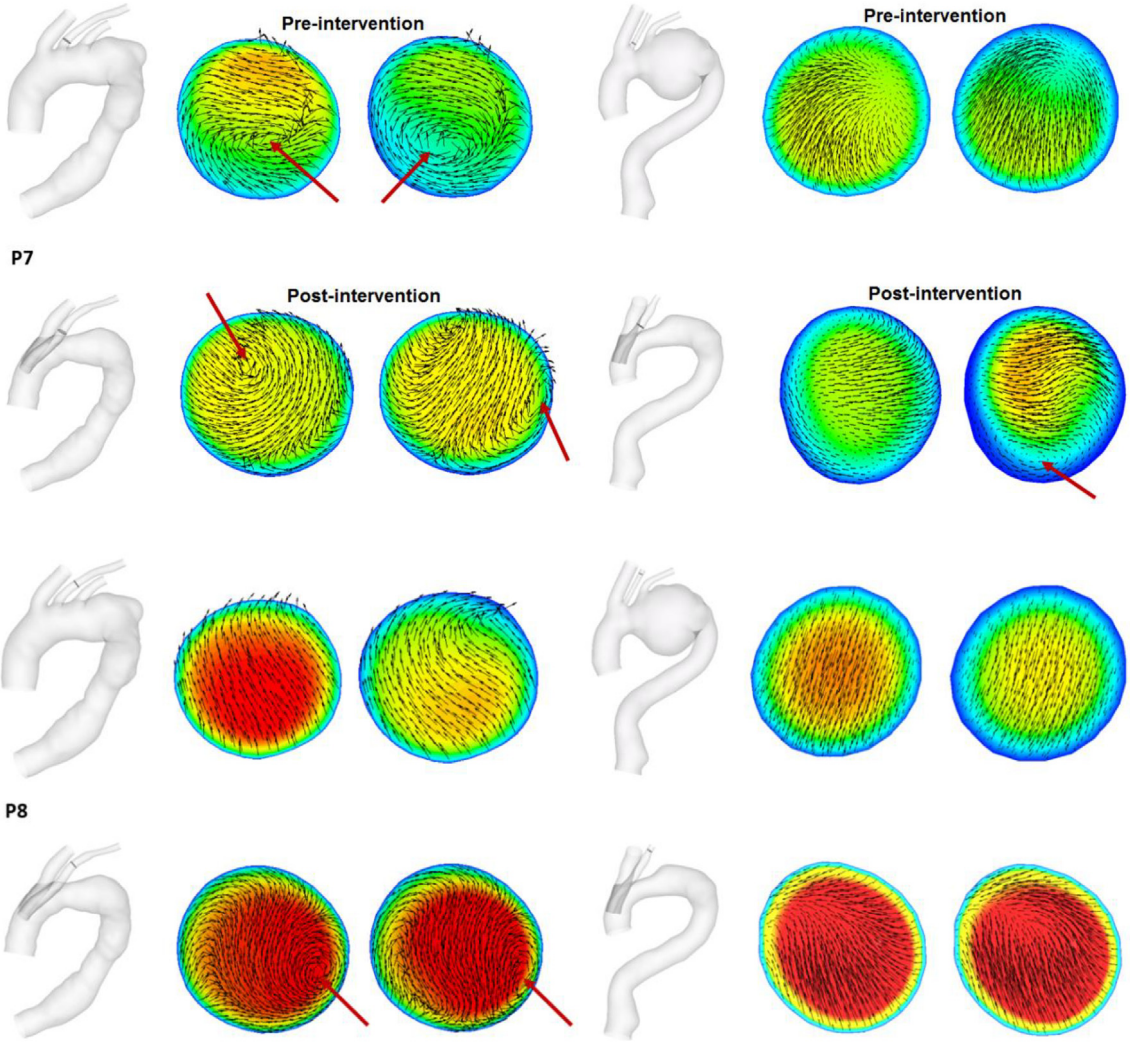

Fig. 5. (*continued*).

cycle.

Fig. 8 shows the circumferential WSS (CWSS) ranges and their variations during a cardiac cycle, with the maximum range of CWSS being highlighted in red. This range determines the value for SRI, which can be used to quantify the degree of asymmetry in WSS caused by disorganised flow near the arterial wall. For both patients, it was obvious that WSS varied more drastically after intervention with much wider ranges, especially along the main aorta (P1–P4). This was largely attributed to the increased non-uniformity in blood flow caused by the inner tunnels. However, one exception was at P4 of patient 2 where there was little change before and after intervention. WSS ranges also increased in the arch vessels (P5–P8) after intervention except at P7 of patient 2, where WSS was more uniform after intervention.

In order to compare the degree of WSS asymmetry before and after intervention, values for SRI were calculated and the results are summarised in Table 2. For patient 1, it is clear that SRI in the aorta increased significantly after intervention, especially at P2 where SRI was nearly 6 times of its pre-intervention value. However, one exception was in the distal LCCA (P8) where SRI was lower in the post-intervention model. For patient 2, SRI values increased in the ascending aorta and arch vessels after intervention but decreased in the distal arch (P3) and the descending aorta (P4).

3.3. Displacement force

Displacement forces acting on the branched endografts were calculated for both patients and their maximum and cycle-averaged values were 21.91 N and 17.85 N for patient 1 and 21.57 N and 17.86 N for patient 2, respectively. The magnitude of displacement force was dominated by pressure as the effect of WSS was less than 1% in these cases.

4. Discussion

Endovascular treatment of thoracic aortic aneurysms faces great challenges especially when it involves the aortic arch owing to the complex anatomy. The Bolton Medical's Relay device is appealing for complex aortic arch diseases since it is specially designed for the tight aorta curvature. In order to help assess the functionality of this device, a detailed hemodynamic analysis was performed in this study based on patient-specific anatomical data and physiologically realistic boundary conditions [34].

Two patients with thoracic aortic aneurysms were included in this study. Results from the pre- and post-intervention models were analysed so that changes in flow conditions could be determined. In the absence of patient-specific information on blood flow, cycle-averaged volumetric flow rate of 5 L/min and 3.4 L/min were applied at the inlets of patient 1 and patient 2, respectively, with 30% of these leaving the aortic arch through the supra-aortic branches [35]. Flow divisions among the IA,

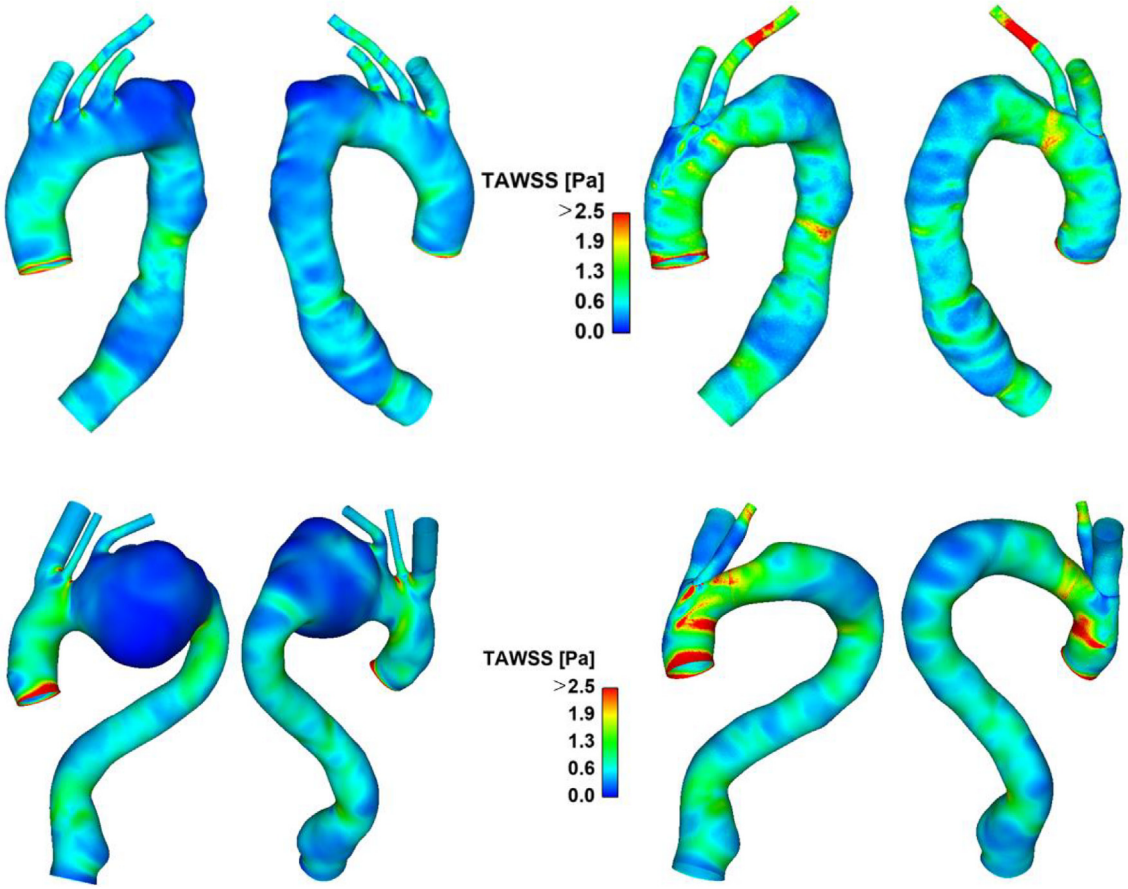

Fig. 6. Comparison of TAWSS before (left) and after (right) intervention for patient 1 (top) and patient 2 (bottom).

LCCA and LSCA were 18%, 5% and 7%, respectively, in the pre-intervention model of patient 1 and 22%, 3% and 5% for patient 2. After intervention, the coverage of LSCA at its root caused flow redistribution, resulting in 0.91 L/min flow through the IA (18%) and 0.62 L/min through the LCCA (12%) of patient 1, while 0.75 L/min through the IA (22%) and 0.27 L/min through the LCCA (8%) of patient 2. For both patients, blood perfusion to the IA was maintained after intervention. The increased flow into the LCCA after intervention was needed as part of it would be diverted into the LSCA through the bypass.

Changes in flow patterns between the pre- and post-intervention models were assessed based on instantaneous velocity streamlines, axial velocity contours and in-plane velocity vectors. As shown in Figs. 4 and 5, the large flow recirculation zone (FRZ) observed in the pre-intervention aneurysm sacs were absent in the post-intervention models. FRZ is characterized by low velocities and flow reversal, which may favour thrombus formation, leading to partial or complete obstruction of the vessel [5]. Therefore, FRZs should be avoided as much as possible. For both patients, away from the regions covered by the stent-grafts, flow in the proximal ascending aorta and the descending aorta were hardly affected by the intervention. In the supra-aortic branches, blood flow was slightly more uniform in the proximal segments due to the smoother transition from the arch in the post-intervention models. Flow in the LCCA of both patients were increased and locally accelerated flow were more obvious in the distal LCCA, since the distal diameters were smaller compared to the slightly oversized stent-grafts in the proximal regions, which were intended to prevent from device migration.

Owing to increased blood velocities in the distal ascending aorta and the arch, wall shear stress (WSS) in the post-intervention aortas was much higher than in the pre-intervention models for both patients, as can be seen in Figs. 6 and 7 for TAWSS and the mean CWSS, respectively. WSS is known to influence endothelial cell functions and gene expression, and is associated with vascular remodelling [36–38]. More specifically, low WSS (<0.4 Pa) has been reported to promote thrombus formation and induce intimal thickening. It was noted that patient 1, whose endograft has equal inner tunnel diameters (15 mm), had low TAWSS around the anastomosis between the inner branches and the main stent-graft. These regions are expected to be thrombosed quickly after TEVAR, which would not cause adverse clinical consequences. However, there was a dramatic reduction in TAWSS in the LCCA of patient 2, whose endograft has smaller inner LCCA tunnel (9 mm) than the IA branch (17 mm), which might increase the risk of thrombus formation in this branch. Similar results were reported by van Bakel et al. [22], who computationally compared different endograft designs for zone 0 aortic arch repair, including two designs similar to the device used in this study. By comparing the two designs, they also found that endograft with a smaller LCCA inner tunnel diameter showed higher risk of thrombosis in the supra-aortic vessels, though not significant.

With regards to the circumferential distribution of WSS, which was measured using SRI (Table 3), the post-intervention ascending aortas of both patients showed significantly higher values of SRI, where blood flow were skewed by the presence of inner tunnels. For patient 1, increased SRI values were also observed in the arch, descending aorta and supra-aortic branches, except for the distal LCCA where flow was more uniform and accelerated, which led to higher mean CWSS and lower SRI values. In contrast to patient 1, SRI values in the distal arch and descending aorta of patient 2 were reduced after intervention where the mean CWSS values were higher than in the pre-intervention model.

Device migration and future complications, such as type I endoleaks, are associated with pressure and wall shear stress experienced by the stent-graft as blood flows through. It has been suggested that a threshold value of approximately 32 N would be needed to dislocate a non-planar

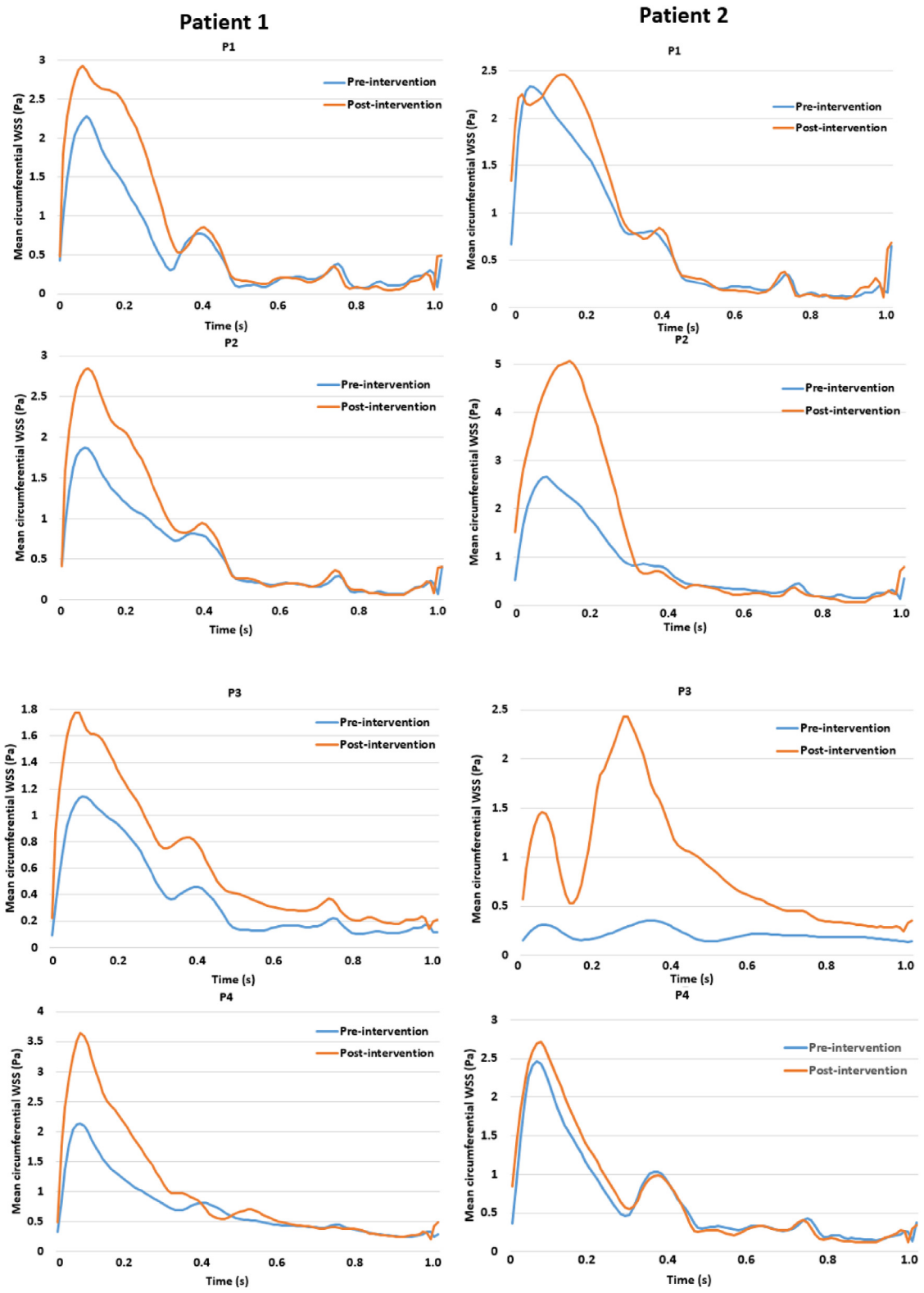

Fig. 7. Comparison of circumferential-averaged wall shear stress (CWSS) at different planes before and after intervention for patient 1 (left) and patient 2 (right).

stent-graft [39], which is well above the maximum displacement forces of 21.91 N and 21.57 N experienced by the branched endografts of patient 1 and patient 2, respectively. Based on these results, it can be deduced that the endografts considered in this study would be at low risk of distal migration.

The present numerical study offered valuable insights into the hemodynamic performance of the branched endograft, but there were some limitations. First, the walls were assumed to be rigid. While this is a reasonable assumption for the relatively stiff endograft, the native aortic wall is compliant and subject to translational motion and radial

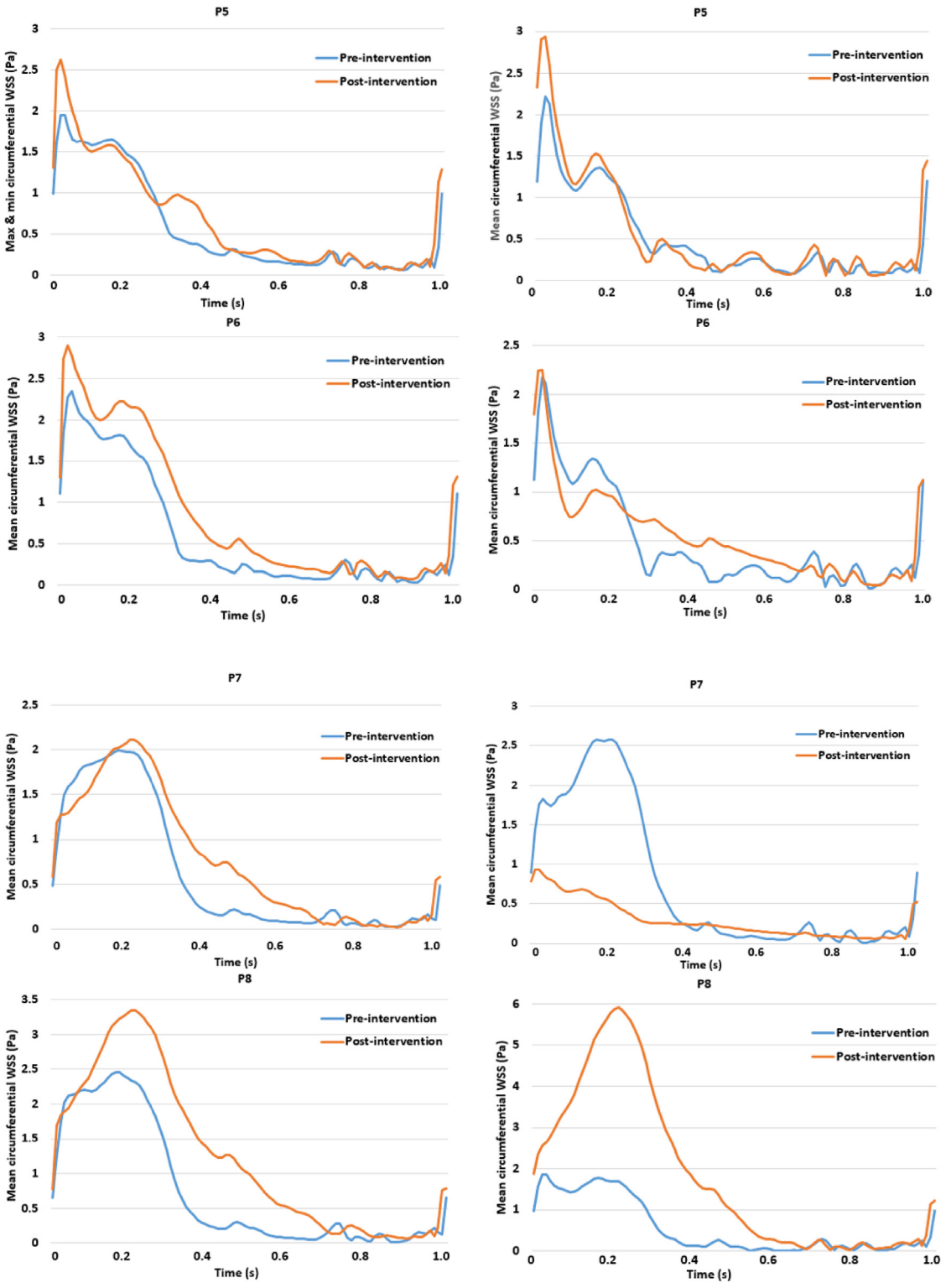

Fig. 7. (*continued*).

expansion. Second, only two cases were analysed, limiting the wider applicability of the findings. Flow patterns and WSS within the IA and LCCA are expected to be influenced by various factors, including inlet velocity profile in the ascending aorta, length and angles between the branches and the aortic arch. Although the main device features are by and large fixed, future studies of more patient cases will be needed to examine a wide variety of anatomical scenarios. Third, inflow and outflow boundary conditions were based on flow and pressure data extracted from the literature as patient-specific flow information was not available for this retrospective study. Finally, there was no direct validation of the results as follow-up data of the two patients are not available. Nevertheless, the same computational methods have been adopted in our previous studies, demonstrating a good overall agreement with available in vivo measurements [8,40,41].

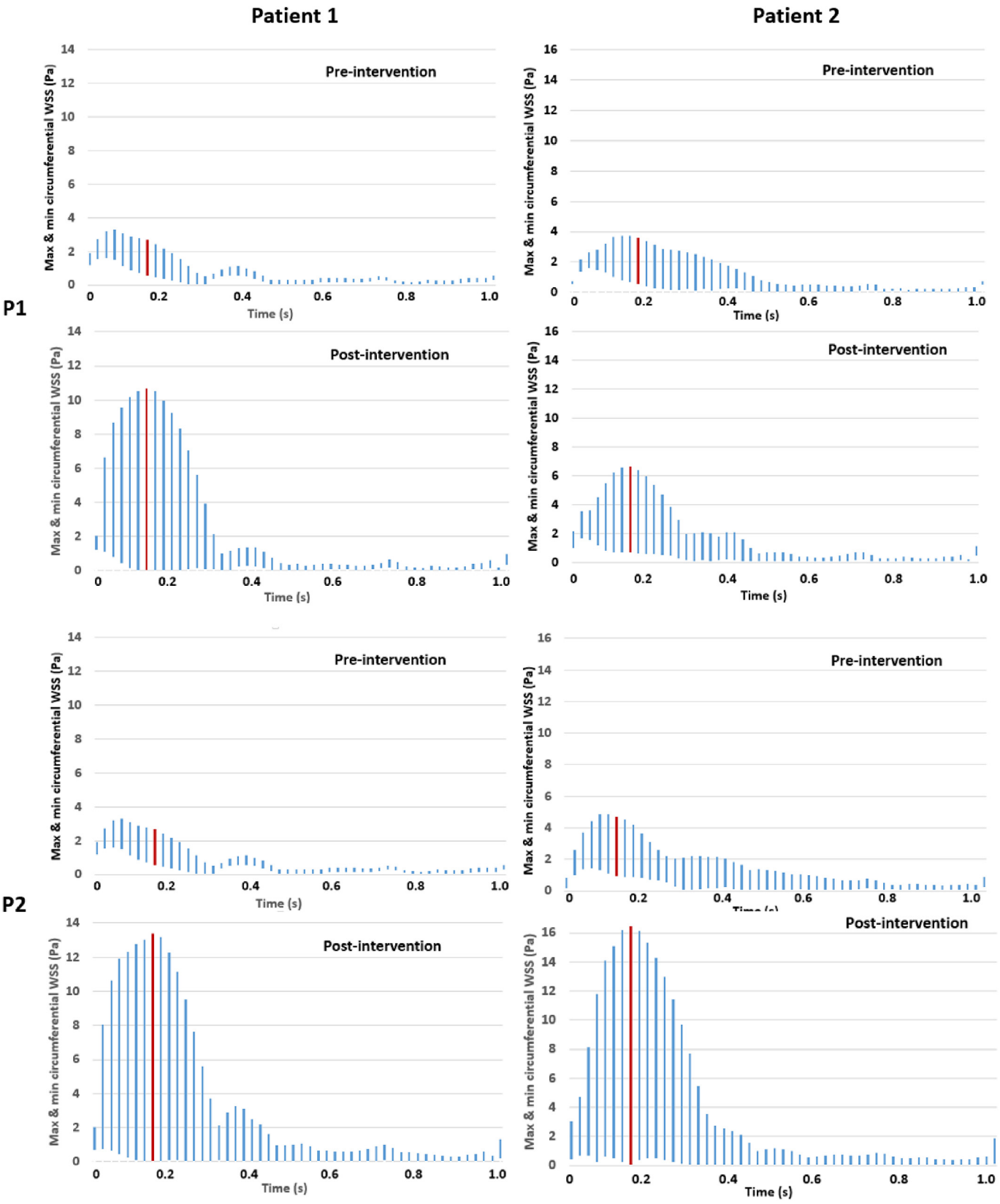

Fig. 8. Comparison of CWSS range in a cardiac cycle before and after intervention for patient 1 (left) and patient 2 (right).

5. Summery

Two thoracic aneurysmal patients were treated with Relay thoracic endografts and detailed hemodynamic conditions, such as flow patterns and WSS related parameters, were evaluated by means of patient-specific computational simulation. First of all, blood flow to the supra-aortic

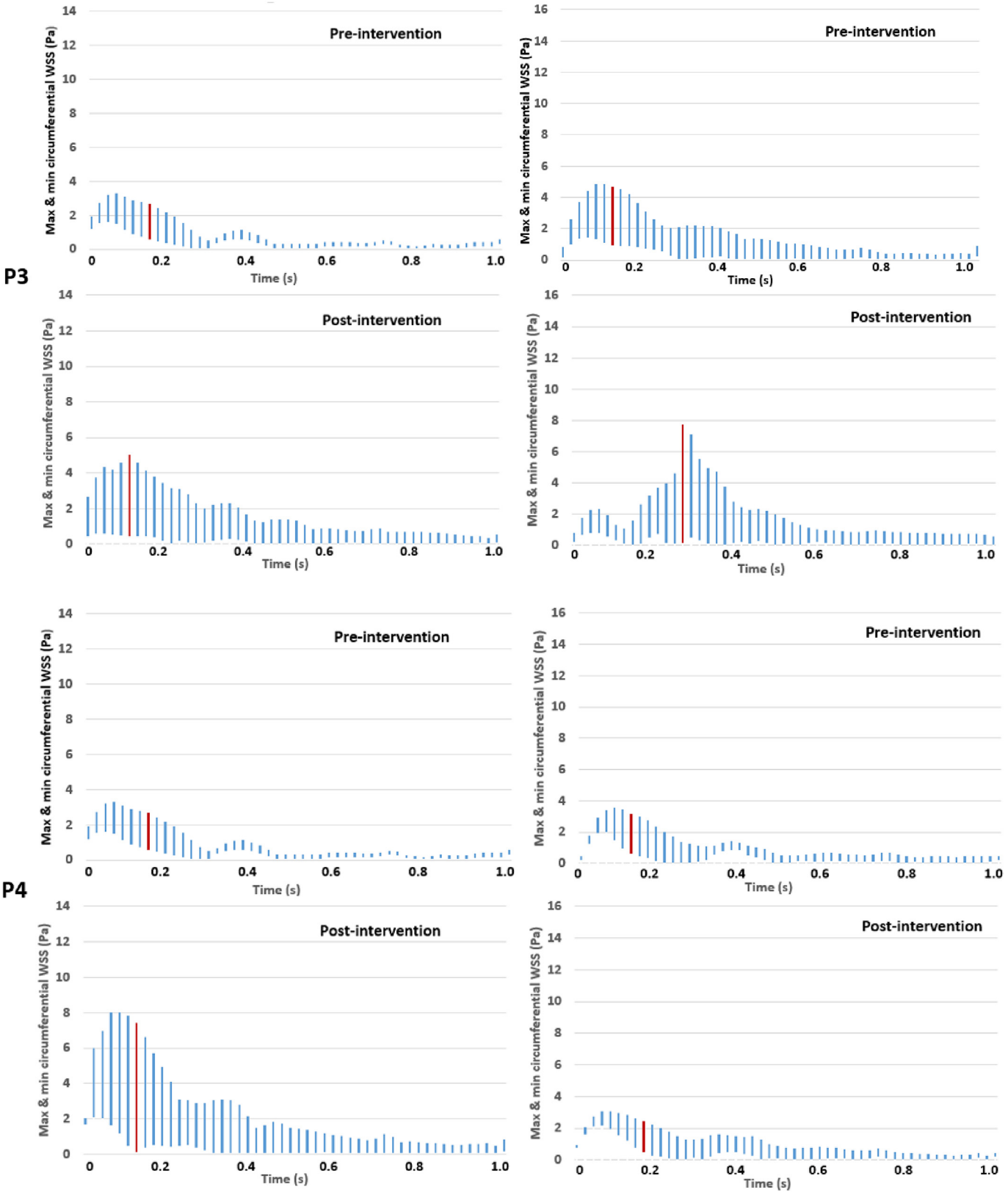

Fig. 8. (*continued*).

branches was found to be sufficient for both patients. Implantation of the device increased TAWSS in the aortic arch due to accelerated blood flow. Elevated TAWSS may help reduce the risk of thrombus formation, but increased spatial variation of WSS and hemodynamic derangement may have a detrimental effect in the long term. This highlights the need for clinical and radiological longitudinal follow up. Moreover, the displacement forces experienced by the endografts were evaluated and the values were below the threshold for device migration. Finally,

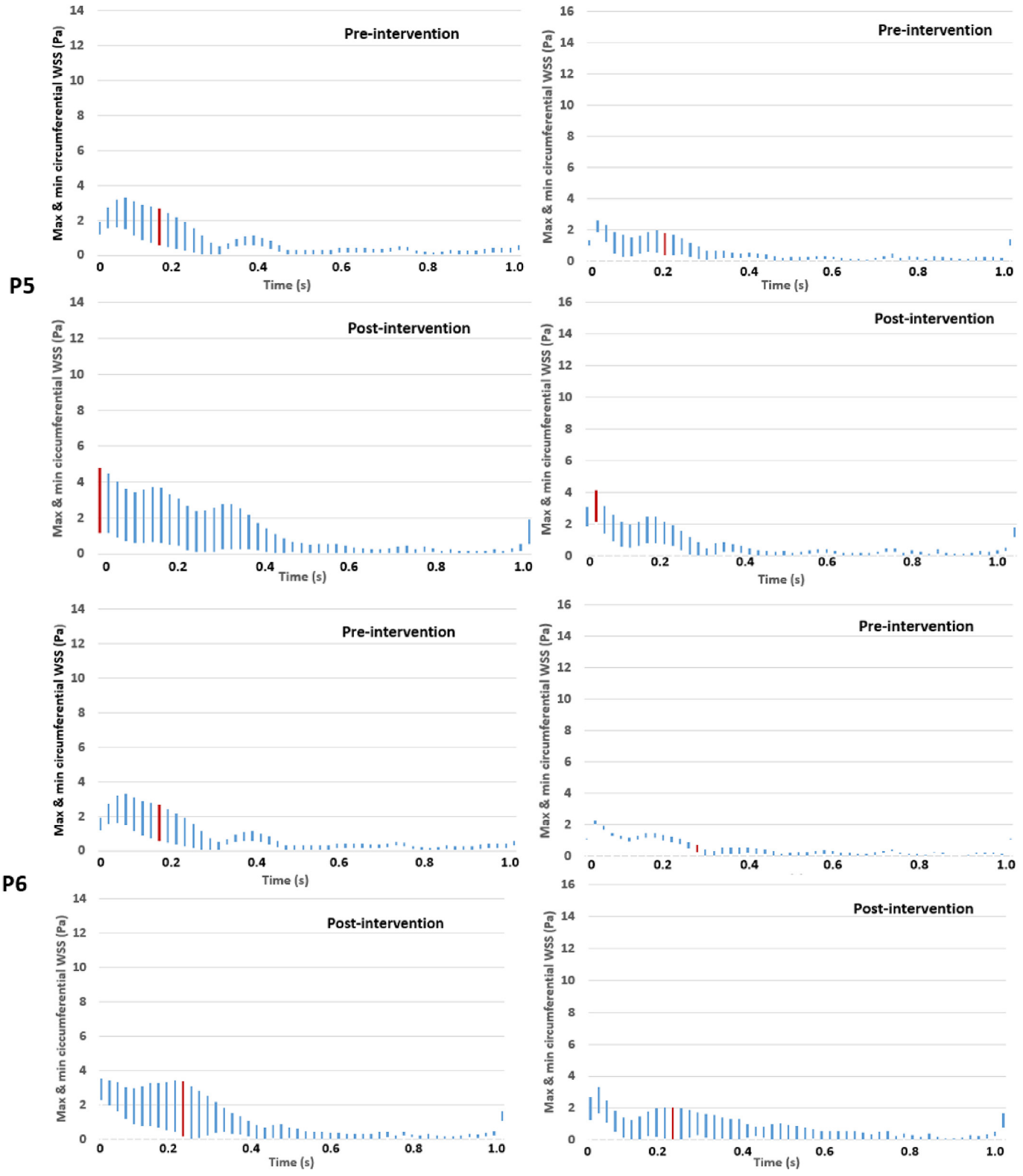

Fig. 8. (*continued*).

branched endograft with a smaller LCCA inner tunnel diameter may increase the risk of thrombosis in the supra-aortic branch. In conclusion, the overall hemodynamic performance of this novel branched endograft is promising, but more patient-specific cases and follow-up studies will be needed to assess the durability of the device.

Ethical approval

All procedures performed in studies involving human participants were in accordance with the ethical standards of the institutional and/or national research committee and with the 1964 Helsinki declaration and its later amendments or comparable ethical standards.

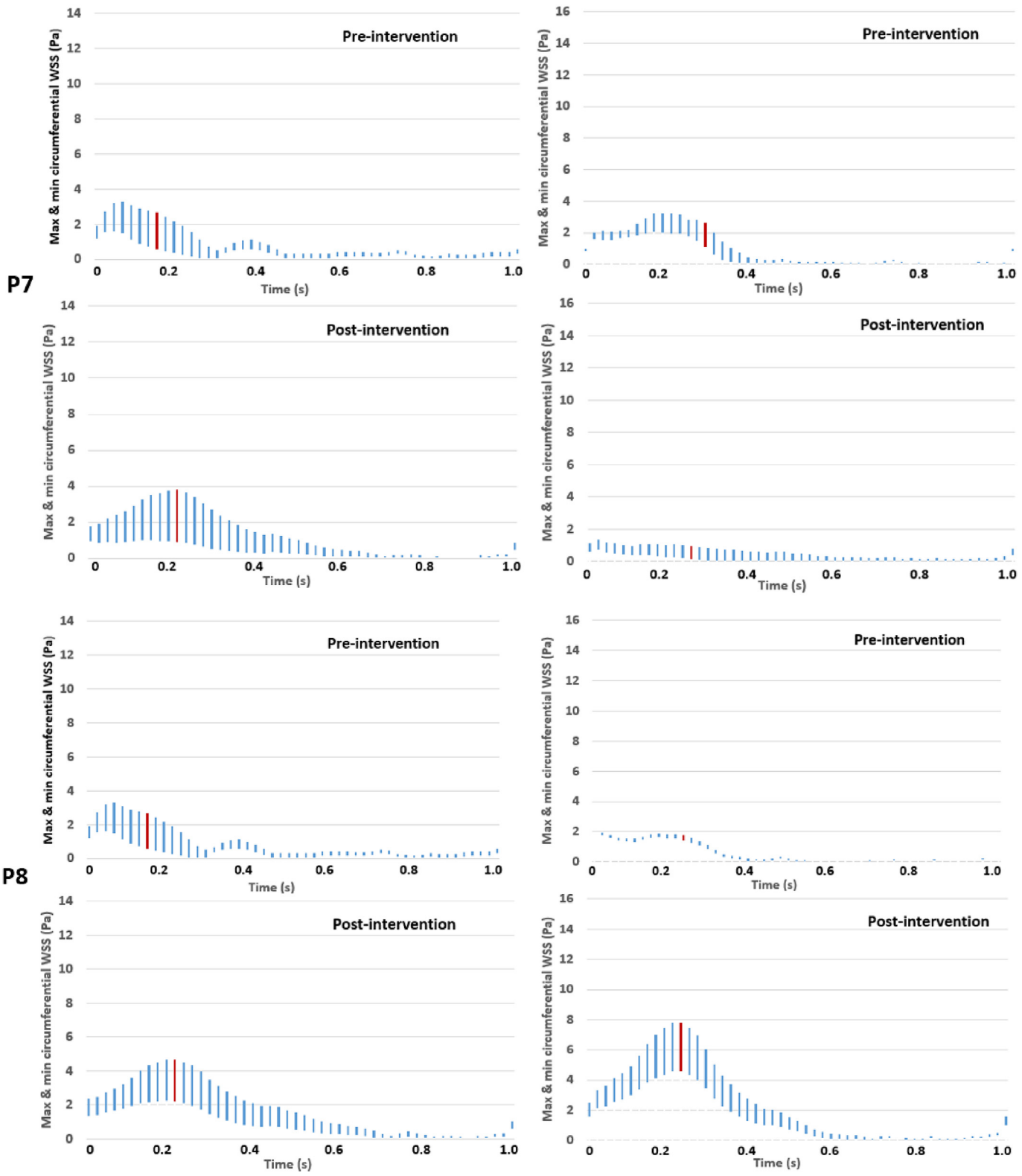

Fig. 8. (*continued*).

Formal ethical approval was not required for this limited retrospective and anonymised study.

Author contribution

Yu Zhu: Methodology, Software, Validation, Formal analysis, Writing- Original draft preparation, Visualization. **Wenbo Zhan**: Methodology, Software, Validation, Formal analysis, Writing- Original draft preparation. **Mohamad Hamady**: Conceptualization, Investigation, Writing- Review & Editing, Resources, Funding acquisition. Xiao Yun Xu: Conceptualization, Investigation, Supervision, Writing- Review & Editing, Resources, Funding acquisition.

Table 3
Comparison of SRI at different locations before and after intervention for both patients.

		P1	P2	P3	P4	P5	P6	P7	P8
Patient 1	Pre-intervention	3.51	2.88	6.15	5.25	2.50	2.14	3.21	2.51
	Post-intervention	12.66	16.44	7.04	7.08	5.19	3.66	3.69	1.94
Patient 2	Pre-intervention	4.24	4.64	9.13	3.78	2.91	0.87	2.04	0.64
	Post-intervention	7.23	12.44	8.38	2.69	3.46	3.72	2.73	1.77

Funding

This work was partially supported by Bolton Medical, Sunrise, Florida, US. The authors declare that although Bolton Medical supported this study, the funding company had no control, in*put or influe*nce on the study design, data analysis or publications.

Declaration of competing interest

MH receives honoraria for scientific talks from Vascutek. Other authors have no conflict of interest to declare.

Acknowledgments

Wenbo Zhan would like to thank Dr Zhuo Cheng for her technical support.

References

[1] van Bogerijen GH, Auricchio F, Conti M, Lefieux A, Reali A, Veneziani A, Tolenaar JL, Moll FL, Rampoldi V, Trimarchi S. Aortic hemodynamics after thoracic endovascular aortic repair, with particular attention to the bird-beak configuration. J Endovasc Ther 2014;21:791–802. https://doi.org/10.1583/14-4778MR.1.

[2] Yunoki J, Kuratani T, Shirakawa Y, Torikai K, Shimamura K, Kin K, Sawa Y. Clinical experience with the RELAY NBS PLUS stent–graft for aortic arch pathology. Surg Today 2014;44:2263–8. https://doi.org/10.1007/s00595-014-0851-2.

[3] Allen BD, Barker AJ, Kansal P, Collins JD, Carr JC, Malaisrie SC, Markl M. Impact of aneurysm repair on thoracic aorta hemodynamics. Circulation 2013;128:e341–3. https://doi.org/10.1161/CIRCULATIONAHA.112.000850.

[4] Markl M, Draney MT, Hope MD, Levin JM, Chan FP, Alley MT, Pelc NJ, Herfkens RJ. Time-resolved 3-dimensional velocity mapping in the thoracic aorta: visualization of 3-directional blood flow patterns in healthy volunteers and patients. J Comput Assist Tomogr 2004;28:459–68. https://doi.org/10.1016/j.jtcvs.2004.08.056.

[5] Kandail H, Hamady M, Xu XY. Comparison of blood flow in branched and fenestrated stent-grafts for endovascular repair of abdominal aortic aneurysms. J Endovasc Ther 2015;22:578–90. https://doi.org/10.1177/1526602815587261.

[6] Taylor CA, Figueroa CA. Patient-specific modeling of cardiovascular mechanics. Annu Rev Biomed Eng 2009;11:109–34. https://doi.org/10.1146/annurev.bioeng.10.061807.160521.

[7] Cheng Z, Kidher E, Jarral OA, O'Regan DP, Wood NB, Athanasiou T, Xu XY. Assessment of hemodynamic conditions in the aorta following root replacement with composite valve-conduit graft. Ann Biomed Eng 2016;44:1392–404. https://doi.org/10.1007/s10439-015-1453-x.

[8] Cheng Z, Juli C, Wood NB, Gibbs RGJ, Xu XY. Predicting flow in aortic dissection: comparison of computational model with PC-MRI velocity measurements. Med Eng Phys 2014;36:1176–84. https://doi.org/10.1016/j.medengphy.2014.07.006.

[9] Singh SD, Xu XY, Wood NB, Pepper JR, Izgi C, Treasure T, Mohiaddin RH. Aortic flow patterns before and after personalised external aortic root support implantation in Marfan patients. J Biomech 2016;49:100–11. https://doi.org/10.1016/j.jbiomech.2015.11.040.

[10] Mori D, Yamaguchi T. Computational fluid dynamics modeling and analysis of the effect of 3-D distortion of the human aortic arch, comput. Methods Biomech. Biomed. Eng. 2002;5:249–60. https://doi.org/10.1080/10255840290010698.

[11] Tse KM, Chang R, Lee HP, Lim SP, Venkatesh SK, Ho P. A computational fluid dynamics study on geometrical influence of the aorta on haemodynamics. Eur J Cardiothorac Surg 2013;43:829–38. https://doi.org/10.1093/ejcts/ezs388.

[12] Tokuda Y, Song MH, Ueda Y, Usui A, Akita T, Yoneyama S, Maruyama S. Three-dimensional numerical simulation of blood flow in the aortic arch during cardiopulmonary bypass. Eur J Cardiothorac Surg 2008;33:164–7. https://doi.org/10.1016/j.ejcts.2007.11.021.

[13] Numata S, Itatani K, Kanda K, Doi K, Yamazaki S, Morimoto K, Manabe K, Ikemoto K, Yaku H. Blood flow analysis of the aortic arch using computational fluid dynamics. Eur J Cardiothorac Surg 2016;49:1578–85. https://doi.org/10.1093/ejcts/ezv459.

[14] Pirola S, Jarral OA, O'Regan DP, Asimakopoulos G, Anderson JR, Pepper JR, Athanasiou T, Xu XY. Computational study of aortic hemodynamics for patients with an abnormal aortic valve: the importance of secondary flow at the ascending aorta inlet. APL Bioeng 2018;2:026101. https://doi.org/10.1063/1.5011960@apb.2019.BOH2019.issue-1.

[15] Gao F, Guo Z, Sakamoto M, Matsuzawa T. Fluid-structure interaction within a layered aortic arch model. J Biol Phys 2006;32:435–54. https://doi.org/10.1007/s10867-006-9027-7.

[16] Tan FPP, Torii R, Borghi A, Mohiaddin RH, Wood NB, Xu XY. Fluid-structure interaction analysis of wall stress and flow patterns in a thoracic aortic aneurysm. Int. J. Appl. Mechanics. 2009;1:179–99. https://doi.org/10.1142/S1758825109000095.

[17] Gao F, Ohta O, Matsuzawa T. Fluid-structure interaction in layered aortic arch aneurysm model: assessing the combined influence of arch aneurysm and wall stiffness. Australas Phys Eng Sci Med 2008;31:32. https://doi.org/10.1007/BF03178451.

[18] Miyazaki S, Itatani K, Furusawa T, Nishino T, Sugiyama M, Takehara Y, Yasukochi S. Validation of numerical simulation methods in aortic arch using 4D Flow MRI. Heart Ves 2017;32:1032–44. https://doi.org/10.1007/s00380-017-0979-2.

[19] Nardi A, Avrahami I. Approaches for treatment of aortic arch aneurysm, a numerical study. J Biomech 2017;50:158–65. https://doi.org/10.1016/j.jbiomech.2016.11.038.

[20] Midulla M, Moreno R, Baali A, Chau M, Negre-Salvayre A, Nicoud F, Pruvo JP, Haulon S, Rousseau H. Haemodynamic imaging of thoracic stent-grafts by computational fluid dynamics (CFD): presentation of a patient-specific method combining magnetic resonance imaging and numerical simulations. Eur Radiol 2012;22:2094–102. https://doi.org/10.1007/s00330-012-2465-7.

[21] Konoura C, Yagi T, Nakamura M, Iwasaki K, Qian Y, Okuda S, Yoshitake A, Shimizu H, Yozu R, Umezu M. Numerical analysis of blood flow distribution in 4- and 3-branch vascular grafts. J Artif Organs 2013;16:157–63. https://doi.org/10.1007/s10047-013-0694-4.

[22] van Bakel TM, Arthurs CJ, van Herwaarden JA, Moll FL, Eagle KA, Patel HJ, Trimarchi S, Figueroa CA. A computational analysis of different endograft designs for Zone 0 aortic arch repair. Eur J Cardiothorac Surg 2018;54:389–96. https://doi.org/10.1093/ejcts/ezy068.

[23] Resch T, Koul B, Dias NV, Lindblad B, Ivancev K. Changes in aneurysm morphology and stent-graft configuration after endovascular repair of aneurysms of the descending thoracic aorta. J Thorac Cardiovasc Surg 2001;122:47–52. https://doi.org/10.1067/mtc.2001.113025.

[24] Nesbitt M, Westein E, Tovar-Lopez F, Tolouei E, Mitchell A, Fu J, Carberry J, Foras A, Jackson S. A shear gradient-dependent platelet aggregation mechanism drives thrombus formation. Nat Med 2009;15:665–73. https://doi.org/10.1038/nm.1955.

[25] Menichini C, Xu XY. Mathematical modelling of thrombus formation in idealised models of aortic dissection: initial findings and potential applications. J Math Biol 2016;73:1205–26. https://doi.org/10.1007/s00285-016-0986-4.

[26] Kandail H, Hamady M, Xu XY. Patient-specific analysis of displacement forces acting on fenestrated stent grafts for endovascular aneurysm repair. J Biomech 2014;47:3546–54. https://doi.org/10.1016/j.jbiomech.2014.08.011.

[27] Kousera CA, Wood NB, Seed WA, Torii R, O'Regan D, Xu XY. A numerical study of aortic flow stability and comparison with in vivo flow measurements. J Biomech Eng 2013;135:011003. https://doi.org/10.1115/1.4023132.

[28] Critchley LAH, Critchley JAJH. A meta-analysis of studies using bias and precision statistics to compare cardiac output measurement techniques. J Clin Monit Comput 1999;15:85–91. https://doi.org/10.1023/A:1009982611386.

[29] Vignon-Clementel IE, Figueroa CA, Jansen KE, Taylor CA. Outflow boundary conditions for 3D simulations of non-periodic blood flow and pressure fields in deformable arteries. Comput Methods Biomech Biomed Eng 2010;13:625–40. https://doi.org/10.1080/10255840903413565.

[30] Olufsen MS, Peskin CS, Kim WY, Pedersen EM, Nadim A, Larsen J. Numerical simulation and experimental validation of blood flow in arteries with structured-tree outflow conditions. Ann Biomed Eng 2000;28:1281–99. https://doi.org/10.1114/1.1326031.

[31] Mohrman D, Heller LJ. Cardiovascular Physiology. McGraw-Hill Medical; 2006.

[32] Kandail H, Hamady M, Xu XY. Effect of a flared renal stent on the performance of fenestrated stent-grafts at rest and exercise conditions. J Endovasc Ther 2016;23:809–20. https://doi.org/10.1177/1526602816651425.

[33] Barker AJ, Lanning C, Shandas R. Quantification of hemodynamic wall shear stress in patients with bicuspid aortic valve using phase-contrast MRI. Ann Biomed Eng 2010;38:788–800. https://doi.org/10.1007/s10439-009-9854-3.

[34] Pirola S, Cheng Z, Jarral OA, O'Regan DP, Pepper JR, Athanasiou T, Xu XY. On the choice of outlet boundary conditions for patient-specific analysis of aortic flow using computational fluid dynamics. J Biomech 2017;60:15–21. https://doi.org/10.1016/j.jbiomech.2017.06.005.

[35] Alastruey J, Xiao N, Fok H, Schaeffter T, Figueroa CA. On the impact of modelling assumptions in multi-scale, subject-specific models of aortic haemodynamics. J R Soc Interface 2016;13:20160073. https://doi.org/10.1098/rsif.2016.0073.

[36] Reneman RS, Arts T, Hoeks APG. Wall shear stress – an important determinant of endothelial cell function and structure – in the arterial system in vivo. J Vasc Surg 2006;43:251–69. https://doi.org/10.1159/000091648.
[37] Levick JR. An Introduction to Cardiovascular Physiology. Butterworth Heinemann; 2013.
[38] Malek AM, Alper SL, Izumo S. Hemodynamic shear stress and its role in atherosclerosis. J Am Med Assoc 1999;282:2035–42. https://doi.org/10.1001/jama.282.21.2035.
[39] Rahmani S, Grewal IS, Nabovati A, Doyle MG, Roche-Nagle G, Tse LW. Increasing angulation decreases measured aortic stent graft pullout forces. J Vasc Surg 2016; 63:493–9. https://doi.org/10.1016/j.jvs.2014.06.115.
[40] Menichini C, Cheng Z, Gibbs RGJ, Xu XY. A computational model for false lumen thrombosis in type B aortic dissection following thoracic endovascular repair. J Biomech 2018;66:36–43. https://doi.org/10.1016/j.jbiomech.2017.10.029.
[41] Pirola S, Guo B, Menichini C, Saitta S, Fu W, Dong Z, Xu XY. 4-D flow MRI-based computational analysis of blood flow in patient-specific aortic dissection. IEEE Trans Biomed Eng 2019;66:3411–9. https://doi.org/10.1109/TBME.2019.2904885.